Annals of the New York Academy of Sciences

ANNALS OF THE NEW YORK ACADEMY OF SCIENCES

ORIGINAL ARTICLE

Three-Dimensional Ribbon-Like Gold Nanoparticle Assemblies on MXene for Detection of Creatinine by Surface-Enhanced Raman Scattering

Lin Chen[1] | Dong Yang[2] | Wanlin Wang[3] | Hongyun Xing[3] | Xianglong Bian[1] | Hua Pei[1] | Qianfeng Xia[1] | Penghui Li[4] | Paul K. Chu[5] | Tingwei Hu[1]

[1]NHC Key Laboratory of Tropical Disease Control, School of Tropical Medicine, Hainan Medical University, Haikou, Hainan, China | [2]School of Biomedical Information and Engineering, Hainan Medical University, Haikou, Hainan, China | [3]School of Physical Sciences, Great Bay University, Dongguan, Guangdong, China | [4]Institute of Biomedicine and Biotechnology, Shenzhen Institutes of Advanced Technology, Chinese Academy of Sciences, Shenzhen, Guangdong, China | [5]Department of Physics, Department of Materials Science and Engineering, and Department of Biomedical Engineering, City University of Hong Kong, Kowloon, Hong Kong, China

Correspondence: Penghui Li (ph.li@siat.ac.cn) | Paul K. Chu (paul.chu@cityu.edu.hk) | Tingwei Hu (htingwei1236@mail.xjtu.edu.cn)

Received: 3 June 2025 | **Revised:** 23 August 2025 | **Accepted:** 25 August 2025

Funding: This work was jointly supported by the National Natural Science Foundation of China (Grant 82472150), the Hainan Provincial Natural Science Foundation of China (Grant 521RC555), Talent Researching Funds (Grants XRC200016, RC2400001279), City University of Hong Kong Donation Research Grants (Grants DON-RMG 9229021 and 9220061), and Hainan Medical University Research Foundation (Grant XSTS2025033).

Keywords: creatinine detection | interfacial self-assembly | MXene | ribbon-like gold nanoparticle assemblies | surface-enhanced Raman scattering

ABSTRACT

Creatinine is an important indicator of renal function, and its accurate and efficient detection is important to clinical diagnosis and disease monitoring. As the structure combining MXene layers and gold nanoparticles (AuNPs) provides many active sites and hot spots for surface-enhanced Raman scattering (SERS), ultrasensitive detection of creatinine can be realized. Herein, homogeneous ultrathin Ti_3C_2-MXene films are produced on a large scale by interfacial self-assembly, and a uniformly distributed AuNP monolayer and three-dimensional ribbon-like AuNP assemblies (RAuNPs) are then separately assembled on the MXene surface by simply regulating the nanoparticle concentration and the drying temperature. The two SERS substrates of AuNPs/MXene and RAuNPs/MXene are capable of sensitive detection of creatinine in aqueous solutions without labels. The SERS activity is verified using Rhodamine 6G (R6G). In the SERS detection of creatinine, the AuNPs/MXene substrate shows a linear range from 1×10^{-4} to 1×10^{-8} M with a limit of detection (LOD) of 287 nM, whereas the RAuNPs/MXene substrate exhibits a good linear relationship in the range from 1×10^{-3} to 1×10^{-10} M with a LOD of 2.64 nM. The outstanding SERS properties of RAuNPs/MXene suggest promising potential pertaining to the rapid and sensitive detection of creatinine.

1 | Introduction

Chronic kidney disease has become a global health problem and impacts the quality of life and socio-economic burden of patients [1]. Creatinine is the waste product of muscle metabolism primarily excreted through the kidneys. The creatinine level in the human body can reflect the detoxification ability and functional status of the kidney and is a widely recognized and

Lin Chen and Dong Yang contributed equally to this work and are co-first authors.

routine biomarker for the early diagnosis of kidney function and kidney disease. The Jaffe method, enzymatic method, and isotope dilution liquid chromatography–mass spectrometry are the common clinical methods for creatinine detection. The Jaffe method is straightforward and economical, but it is susceptible to interference from some non-specific reducing substances in human blood, such as acetone, pyruvate, vitamin C, and glucose. These substances can react with basic picric acid to produce a red color, which interferes with the detection of serum creatinine [2]. The enzymatic method has high specificity and anti-interference ability for creatinine detection. However, it is quite expensive [3], and phenol sulfonamide and calcium hydroxybenzoate (CaD) used in the test can render results unreliable [4]. Although isotope dilution liquid chromatography–mass spectrometry is an accurate method for creatinine detection, it requires special equipment, and the associated cost is high [5]. With the increasing demand for clinical detection of creatinine, the limitations of these methods have made them inadequate; thus, a simple, fast, sensitive, and economical creatinine detection method is highly desirable.

As surface-enhanced Raman scattering (SERS) can realize fast fingerprint detection without labeling [6–8], it has many advantages in practical applications [9], such as food safety [10, 11], environmental monitoring [12, 13], and biomedicine [14–19]. There are two enhancing mechanisms, namely, electromagnetic (EM) enhancement and chemical (CM) enhancement. The dominant mechanism of EM originates from the local surface plasmon resonance (LSPR) effect. LSPR is a unique physical phenomenon on the surface of noble metal nanoparticles (such as gold, silver, and copper). When the frequency of the incident light matches the intrinsic oscillation frequency of the free electrons in the particles, it will excite resonance and significantly enhance the local EM field [20–22]. When the target molecule is located in the enhanced field region, its Raman signal can be efficiently amplified. CM mainly originates from the strong interaction between the target molecule and the SERS substrate. Such effects increase the polarizability and Raman scattering cross section of molecules by altering their electron density. Under laser excitation, the change in electron density further induces charge transfer. If the excitation light energy resonates with the charge transfer state of the target molecular-substrate composite system, a significant enhancement effect will occur. The charge transfer theory is the core mechanism of CM enhancement and provides a key theoretical basis [23, 24]. In the enhancement mechanism of SERS, EM is generally regarded as the main contributing factor [25]. Although SERS detection of creatinine with noble metal substrates has been reported [26, 27], the detection sensitivity needs to be improved. For example, Wen et al. have prepared a nano-Ag/Au@Au membrane by the liquid–liquid interface self-assembly method showing a creatinine detection limit of 5×10^{-6} M [26]. Zhang et al. have determined creatinine using optimal hot spots produced by gold nanocubes with a limit of detection (LOD) of 44 nM [27].

The combination of noble metal nanoparticles and two-dimensional (2D) nanomaterials can generate synergistic EM and CM enhancement and contributes to more satisfactory SERS performance [14, 28, 29]. Among these 2D nanomaterials, MXene are emerging candidates for SERS with the CM mechanism due to their excellent CM stability and charge transfer [30, 31]. To be specific, MXene possess metallic properties, surface plasmon resonance (SPR), hydrophilicity, high transmittance, large specific surface area, rich surface chemistry, tunable electronic structure, and low production costs, all of which contribute to enhancing the sensitivity of SERS detection [31, 32]. Moreover, their hydrophilic surfaces enable the adsorption of a wide range of CM substances, such as biotoxins [33] and amino acids [15], significantly amplifying the SERS signals of these molecules and thus achieving more sensitive and powerful CM analysis. Shao et al. developed a SERS substrate based on the Ag/ZIF-67 cage@MXene (AZMC) heterostructure, which utilizing MXene's large surface area to host noble metals and bond ZIF-67 with MXene via Co–O–Ti bonding, forming a heterojunction that enhances stability and suppresses oxidation, and exhibiting excellent SERS performance [34]. Xie et al. have prepared gold nanorods on MXene layers, and the SERS substrate shows high sensitivity in the detection of several molecules [35]. Yang et al. demonstrated a photocatalytic in situ synthesis of AuNPs on MXene, achieving enhanced SERS performance with an ultra-low LOD of 10^{-9} M for benzimidazole pesticides and structurally analogous contaminants [36]. These works not only confirm the contribution of combined EM/CM enhancement but also corroborate the CM mechanism of MXene layers as enhanced molecule capture and electron transfer [32]. However, in these composite nanostructures, the noble metal nanoparticles are randomly aggregated or attached on the MXene layers, or with monolayer covered on the MXene forming a 2D thin film [14, 35, 37, 38]. These structures result in the randomly dispersed EM field or limited SERS hotspots, hampering the maximization of the EM enhancement in the EM/CM synergistic mechanism. There have been no reports on the three-dimensional (3D) uniformly arranged gold nanoparticle (AuNPs) assemblies on MXene.

3D structured SERS substrates exhibit numerous advantages [39, 40]. Their complex 3D morphology optimizes EM field distribution, effectively enhancing the SERS signal. Compared to 2D substrates, 3D structures not only provide dense hot spots within the active region but also possess a larger effective surface area, facilitating the adsorption of target molecules and thereby significantly boosting SERS performance and detection sensitivity. Furthermore, the 3D design enhances signal reproducibility and reliability, laying a solid foundation for high-sensitivity and high-stability SERS detection. For instance, Zhao et al. successfully constructed a large-area, 3D hierarchical nanostructure rich in dense hot spots using a two-step physical deposition process [41], which significantly enhanced SERS signal intensity and demonstrated extremely high sensitivity and excellent reproducibility in the detection of Rhodamine 6G (R6G) and melamine. Zhang et al. developed an innovative 3D nanoporous gold/AuNPs (3D-NPG/AuNPs) composite substrate for the highly sensitive and specific detection of 6-benzyladenine and melamine in food [42]. This structure exhibits outstanding uniformity, reproducibility, and stability, providing a rapid, accurate, and highly sensitive new method for food safety testing.

In this work, 3D AuNP assemblies on Ti_3C_2-MXene layers are constructed to create ample active sites and SERS hotspots for a high performance SERS substrate for creatinine detection. First, large-scale and homogeneous Ti_3C_2-MXene ultrathin films are fabricated by the interfacial self-assembly method. The uniformly distributed AuNP monolayer and 3D ribbon-like AuNP assemblies (RAuNPs) are then separately assembled on the MXene surface by simply regulating the nanoparticle concentration and the drying temperature. AuNPs/MXene and RAuNPs/MXene are prepared for the detection of creatinine in aqueous solutions without labels. The SERS activity is evaluated by the Raman probe molecule of R6G, and the RAuNPs/MXene substrate is verified to possess more significant SERS enhancement performance. For the SERS detection of creatinine, the AuNPs/MXene substrate shows a linear detection range from 1×10^{-4} to 1×10^{-8} M with an LOD of 287 nM, whereas the RAuNPs/MXene substrate delivers better performance, showing a linear relationship from 1×10^{-3} to 1×10^{-10} M and an LOD of 2.64 nM.

2 | Experiment Details

2.1 | Chemicals and Materials

Titanium aluminum carbide (Ti_3AlC_2) was purchased from RHAWN Chemical Reagent Co. Ltd. (Shanghai, China). Lithium fluoride (LiF), chloroauric acid ($HAuCl_4 \cdot 3H_2O$, 99.9%), ethyl acetate, trisodium citrate dihydrate, hydroxylamine hydrochloride, polyvinylpyrrolidone, R6G, cyclohexane, ethyl alcohol, and creatinine were purchased from Xilong Chemical Co. Ltd. (Guangdong, China). Concentrated hydrochloric acid (HCl) was purchased from Cologne Chemical Reagent Co. Ltd. (Chengdu, China). All the CMs were analytical grade and used without further treatment.

2.2 | Synthesis and Assembly of Ti_3C_2-MXene Films

Ti_3C_2-MXene was synthesized according to a previously reported process [43]. In brief, Al in Ti_3AlC_2 was selectively etched using a solution of HCl/LiF, and Ti_3C_2 powder was used to fabricate the 2D MXene nanosheets ultrasonically. LiF (3.2 g) was added to 40 mL of HCl (9 M) under stirring at 1200 rpm at 35°C for 15 min. Ti_3AlC_2 (1 g) was added and stirred for 48 h. After etching, the solution was washed with HCl and then DI water to reach a pH of 7.0. Finally, the MXene solution was vacuum-filtered (0.2 μm membrane) to obtain the multiple layers of MXene and then freeze-dried to obtain the MXene powder. As depicted in Figure 1a, the interfacial assembly process of Ti_3C_2-MXene was slightly varied from the previous experiments [44]. The prepared MXene powder was prepared into an aqueous solution of Ti_3C_2-MXene (20 mL, 0.25 mg/mL), then the solution was placed in a glass petri dish and placed in a fume hood. Then 1.0 mL of ethyl acetate (10% v/v) was added. At room temperature, as ethyl acetate evaporated, MXene flakes began to appear. After evaporation, 1.0 mL of HCl (0.1 M) was added to make the pH of the MXene solution to be 2–3. Subsequently, 1.0 mL of ethyl acetate was added again for the interfacial assembly of MXene flakes. Wait for 5 min until the ethyl acetate has completely evaporated, then transfer the floating MXene film onto a silicon (Si) substrate.

2.3 | Preparation of AuNPs/MXene and RAuNPs/MXene

AuNPs were prepared by the seed growth method [45]. The $HAuCl_4$ solution (100 mL, 0.01% w/v) was added into a three-neck flask and placed in a heated magnetic agitator connected to a condensing tube. After heating to 100°C, the sodium citrate dihydrate solution (2 mL, 0.01 g/mL) was added and stirred magnetically for 15 min until the solution changed from light yellow to garnet red. The solution cooled naturally to room temperature under reflux condensation. The prepared sol (25 mL) was added to a new three-neck flask, to which 1.0 mL of trisodium citrate dihydrate solution (0.01 g/mL), 1.0 mL of PVP solution (1% w/v), and 20 mL of hydroxylamine hydrochloride solution (25 mM) were added and stirred at 300 rpm. At the same time, the $HAuCl_4$ solution (20 mL, 0.1% w/v) was dripped into a new three-neck flask through a funnel and then magnetically stirred for 20 min. Upon observing the formation of a gold film on the solution surface and a distinctive color shift from garnet red to dark purple, the mixture was transferred to a refrigerator set at 4°C for subsequent use.

The AuNPs/MXene substrate was crafted by first covering the MXene film with a gold film derived from a low concentration AuNPs solution, a process detailed previously, and then drying it at room temperature. Subsequently, to produce a gold film from a high concentration AuNPs solution, the low concentration solution was centrifuged at 9000 rpm for 10 min. Post-centrifugation, the supernatant was discarded, and the sedimented particles were re-dispersed in 10 mL of ultra-pure water to form a high concentration AuNPs solution. This concentrated solution was then transferred into a beaker, and 1 mL of cyclohexane was gradually introduced to facilitate a comprehensive reaction. Upon completion of the reaction, 1 mL of ethanol was promptly added. As the cyclohexane evaporated, the AuNPs coalesced to form a gold film on the liquid's surface. The RAuNPs/MXene substrate was then prepared by overlaying the MXene film with this high concentration AuNP solution–assembled gold film, followed by subjecting the substrate to a thermal treatment at 150°C. This entire procedure was reiterated three times to achieve a densely packed arrangement of RAuNPs. According to prior studies, the molar extinction coefficient of near 40 nm AuNPs is approximately 8.42×10^9 M^{-1}/cm [46]. The concentrations of AuNP solutions were calculated on the basis of the UV–Vis absorption spectra presented in Figure S1c. Using the Lambert–Beer law, the concentrations of low and high concentration AuNP solutions were calculated to be 0.165 and 0.357 nM, respectively.

2.4 | Materials Characterization

The morphology of MXene and AuNPs was examined by scanning electron microscopy (SEM, ZEISS Sigma 300), transmission electron microscopy (TEM, JEOL JEM-F200), and high-resolution TEM (HR-TEM). The elemental distribution was determined by energy-dispersive x-ray spectroscopy (EDS) on the SEM. Raman scattering was performed on the confocal Raman instrument

(inVia Qontor). The structure of MXene and AuNPs was characterized by x-ray diffraction (XRD, PANalytical X'pert PRO with a standard Cu K_α radiation source). UV–visible spectrophotometer (TU-2910, China).

2.5 | Preparation of R6G and Creatinine Standard Solutions

The R6G powder (0.00479 g) was dissolved in 1.0 mL of ultra-pure water to prepare the aqueous solution with a concentration of 1×10^{-2} M. The R6G solutions with lower concentrations (1×10^{-3} to 1×10^{-12} M) were prepared by double dilution in turn. Similarly, the creatinine powder (11.4 mg) was dissolved into 1.0 mL of ultra-pure water to prepare the aqueous solution with a concentration of 1×10^{-2} M. The creatinine solution was diluted in sequence to prepare solutions with lower concentrations (1×10^{-3} to 1×10^{-11} M).

2.6 | SERS Measurements and Detection of Real Samples

In the SERS measurements, a laser with a wavelength of 633 nm was used as the excitation source together with a 50× objective lens at room temperature. The detection range was 100–2000 cm^{-1}, and the acquisition time was 10 s for each Raman spectrum. Prior to detection, the baseline was calibrated to exclude fluorescence. Three SERS substrates, including AuNPs/Si, AuNPs/MXene, and RAuNPs/MXene, were prepared for creatinine detection. For all three substrates (Si/AuNPs, AuNPs/MXene, and RAuNPs/MXene), the analyte solutions with varying concentrations were uniformly applied by immersing the substrates for a defined duration. After the immersion period, the substrates were air-dried prior to SERS spectral measurement. The locations of RAuNPs could be easily observed under an optical microscope, which facilitates target finding and testing. More than three points were chosen randomly, and the error bar represents the standard deviation of three measurements.

The clinical serum samples were collected after approval by the Ethics Committee of the Second Affiliated Hospital of Hainan Medical University, and written informed consent was obtained from all participants. Randomly selected blood samples were immediately centrifuged at 4000 rpm for 10 min to separate the serum. The supernatant (serum) was then collected, aliquoted into sterile microcentrifuge tubes (150 μL per tube), and stored at 4°C for subsequent use. The method for detecting creatinine in the serum samples was identical to that previously described for creatinine detection in aqueous solutions.

2.7 | Numerical Simulations

The EM field enhancement distribution of AuNPs/MXene and RAuNPs/MXene substrates was performed with COMSOL Multiphysics 5.3. The structures were first sketched using Autodesk Fusion 360 and then imported into COMSOL Multiphysics. A linearly polarized plane wave with the wavelength of the excitation (633 nm) was incident directly upon the plasmonic nanostructures with polarization along the dimer axis. In the simulations, the permittivity of gold was set to $\mathcal{E}_{Au} = -11.740 + 1.2611i$ [47]. The thickness and refractive index values for the MXene films were taken as 10 nm and 2.38, respectively [44, 48, 49]. In the simulations, detailed structural information regarding the AuNPs and their aggregation was derived from TEM images in Figure S1a,b. The diameter of the AuNPs is 38 nm. In the AuNPs/MXene and RAuNPs/MXene substrates, the interparticle gaps between AuNPs are 4.0 and 1.5 nm, respectively. Additionally, the distance between the MXene and the AuNPs is maintained at 3 nm.

3 | Results and Discussion

The AuNP assemblies on MXene layers with two different structures, that is, AuNPs/MXene and RAuNPs/MXene, are fabricated via a two-step liquid–liquid interface self-assembly process, followed by transferring and drying. The whole process starts with the fabrication of the MXene layers on silicon. Ti_3C_2-MXene powder is prepared through the HCl/LiF etching method [43]. Figure 1a displays the schematic illustration of the optimized liquid–liquid interface self-assembly process, in which ultrathin MXene films can be assembled on a large scale. In brief, the MXene dispersion solution is poured onto a glass petri dish, and the ethyl acetate solution is added. Because of the low solubility, a thin layer of ethyl acetate is formed on the solution surface to cause a high vapor pressure, and a temperature gradient and constant turbulence in the MXene solution are generated by Rayleigh–Bénard convection [50]. As a result, the water layer is gradually exposed during continuous evaporation of ethyl acetate to create high surface tension. Due to the Marangoni effect, the MXene sheets begin to assemble on the exposed water surface [44], forming loose ultrathin MXene after complete evaporation of ethyl acetate. The addition of HCl breaks the electrostatic repulsion between individual MXene sheets, and the self-assembled MXene is transferred to a Si substrate.

SEM and TEM are used to characterize the morphological and structural features of the assembled MXene films. Figure 1b shows the SEM image, revealing cracks after transferring to Si. The MXene surface is smooth, albeit showing typical wrinkles from overlapping MXene layers. Figure 1c,d demonstrates the TEM image and the lattice structures of MXene by HR-TEM, disclosing the folds and ultrathin nature, with the lattice spacing of 0.33 nm indicating the $Ti_3C_2T_x$ crystal plane [51]. Figure 1e shows the Raman spectrum of the assembled MXene films. There are five main characteristic peaks at 120, 200, 282, 372, and 615 cm^{-1} of Ti_3C_2-MXene [52, 53]. The Raman peaks at 120 and 200 cm^{-1} stem from vibrations of Ti atoms in $Ti_3C_2F_2$ and $Ti_3C_2O_2$, and that at 615 cm^{-1} comes from C atoms in $Ti_3C_2(OH)_2$ [52, 53]. There is a prominent Raman peak at 200 cm^{-1} of the self-assembled MXene thin film. According to the results of the test by tip-enhanced Raman scattering (TERS) [54], the Raman peak of MXene layer at 200 cm^{-1} indicates the mono-layered feature. Thus, the self-assembled MXene film in this experiment is potentially a single layer.

The AuNPs are synthesized by the seed growth method, and the typical TEM image and absorption spectrum illustrated in Figure S1 suggest the successful synthesis. These AuNPs can form a gold film by the liquid–liquid interface self-assembly, which is transferrable. As shown in Figure 2a, the AuNPs/MXene substrate is

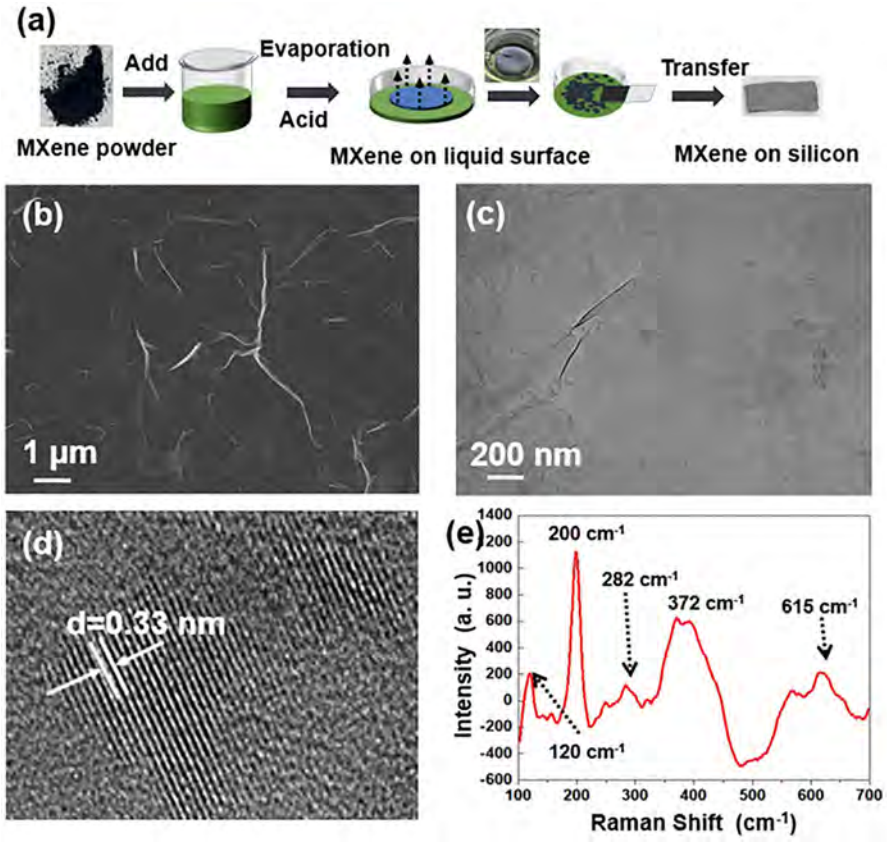

FIGURE 1 | (a) Schematics showing the assembly process of ultrathin MXene films; (b) scanning electron microscopy (SEM) images of MXene films; (c) transmission electron microscopy (TEM) and (d) high-resolution transmission electron microscopy (HR-TEM) images of MXene films; and (e) Raman spectrum of assembled ultrathin MXene films.

prepared by transferring the gold film that is assembled at low concentration AuNPs solution onto the MXene film, followed by drying at room temperature. Figure S2a shows the TEM image of the MXene film decorated with AuNPs that are uniformly distributed on the surface, and Figure S2b displays the lattice structures of MXene and AuNPs obtained by HR-TEM. The lattice spacings of 0.306 and 0.226 nm correspond to the $Ti_3C_2T_x$ crystal plane and the AuNPs, respectively [55, 56]. Figure S2c shows the XRD results of MXene films (black curve) and AuNPs/MXene (red curve). The MXene films show a sharp diffraction peak and a broad peak at 6.44° and 28.34° corresponding to the (0 0 2) and (0 0 8) crystal faces of Ti_3C_2, respectively. AuNPs/MXene show the (0 0 2) peak at 6.44°, whereas AuNPs show peaks at 38.16°, 44.62°, 64.84°, and 77.36°, corresponding to the (1 1 1), (2 0 0), (2 2 0), and (3 1 1) faces of gold, respectively [57]. XRD confirms the $Ti_3C_2T_x$ phase and AuNPs [58].

The morphology of AuNPs/MXene is observed by SEM, as depicted in Figure 2b; a reasonably uniform distribution of AuNPs on MXene ultrathin film is accomplished through assembling gold film at low concentration AuNPs solution, followed by drying at room temperature, albeit with some minimal uncovered areas. Figure 2c reveals a uniform distribution of AuNPs on the flat MXene surface, and Figure 2d shows that the AuNPs are distributed around the MXene wrinkles. Apparently, the distribution of AuNPs on MXene surface can be affected by the wrinkles and functional groups. Although the AuNPs tend to accumulate around the wrinkles of MXene films, it is difficult for them to coalesce into a banding structure. The wrinkle or folds on MXene surface provides a physical limiting space, promoting the aggregation of AuNPs on the surface [59]. The variations in surface energy between the folded and flat regions of MXene can potentially influence the aggregation behavior of AuNPs [60]. The local stress at the folds may also encourage the aggregation of AuNPs. Meanwhile, the diverse functional groups on MXene surface have the potential to engage in interactions with AuNPs, thereby enhancing the adhesion of AuNPs in the wrinkled region [30]. Overall, AuNPs/MXene obtained by the dryness process at room temperature exhibits the structure of a 2D layer of AuNPs uniformly assembled on MXene surface. Figure 2e confirms the uniformly distributed C, O, Ti, Au, and F in the AuNPs/MXene surface, with concentrations of 68.15%, 11.03%, 2.42%, 73.31%, and 2.29%, respectively (Figure S3a).

The RAuNPs/MXene substrate is prepared with a similar method but with different dying conditions. As depicted in Figure 3a, the MXene/RAuNPs substrate is prepared by covering the MXene film with a gold film, followed by a thermal treatment of the substrate at 150°C. In this study, the temperature of 150°C is set for thermal treatment based on previous findings that aggregation of AuNPs is particularly pronounced at this temperature [61]. The change of drying temperature significantly influences the aggregation behavior of AuNPs on the surface of the MXene films, and the obtained assemblies (RAuNPs/MXene) exhibit structures quite different from AuNPs/MXene (Figure 2b–d). This is primarily because the high-temperature thermal treatment

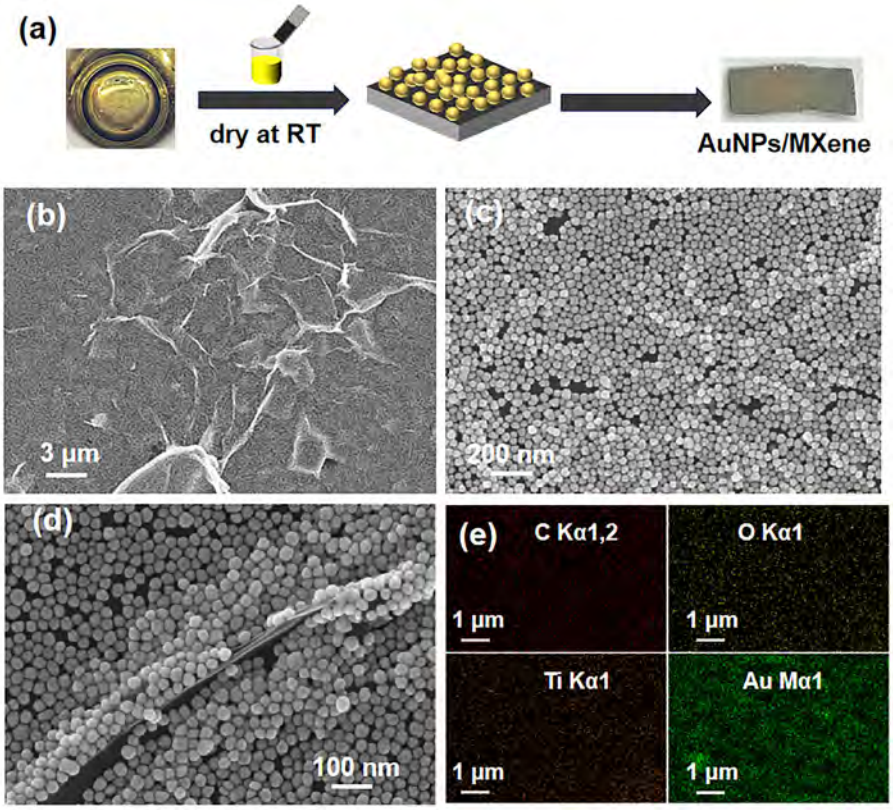

FIGURE 2 | (a) Flow chart showing the preparation process of AuNPs/MXene; (b–d) scanning electron microscopy (SEM) images of AuNPs/MXene; and (e) energy-dispersive x-ray spectroscopy (EDS) elemental maps of AuNPs/MXene.

provides additional thermal energy to the AuNPs, which not only enhances their thermal motion but also increases their kinetic energy. The increase in kinetic energy leads to a higher frequency of collisions between particles, and these factors work together to facilitate the aggregation process [61, 62].

Furthermore, variations in the concentration of AuNPs also influence their aggregation behavior on the MXene film surface. As shown in Figure S4a–c, with the low concentration AuNPs solution, most of the AuNPs are still uniformly dispersed on MXene films, but relatively loose ribbon-like structured assemblies of RAuNPs form in certain areas. With the increase of the AuNPs solution concentration, most of the AuNPs aggregate into more densely packed ribbon-like RAuNPs assemblies (Figure S4d–f), forming the 3D RAuNPs/MXene. This aggregation phenomenon occurs because the high concentration of the AuNPs solution not only raises the frequency of interactions between particles but also increases the degree of aggregation in the final RAuNPs structure [63].

The morphology of RAuNPs/MXene is further examined by SEM, and as shown in Figure 3b and the zoomed images in Figure 3c,d, the AuNPs aggregate along the wrinkles of the MXene film, forming 3D ribbon-like structures with the densely packed arrangement of AuNPs. Moreover, Figure 3e,f illustrates the morphological relationship between the RAuNPs and MXene wrinkles. It is evident that the RAuNPs not only accumulate around the MXene wrinkles but also conform to the wrinkle patterns, adopting shapes that align with them. The interparticle gaps of the AuNPs are also severely compressed, compared to AuNPs/MXene. This observation underscores the direct influence of the MXene wrinkle's shape on the formation and morphology of the RAuNPs, highlighting a significant interplay between the two components. Figure 3g and Figure S5 disclose the presence of C, O, Ti, Au, and F with concentrations of 66.53%, 12.13%, 7.49%, 8.05%, and 5.79%, respectively.

According to absorption spectra and the intensity of different excited lasers, 633 nm laser has been chosen as the excitation source. As shown in Figure S6a, AuNPs show maximum absorbance at 520 nm due to their SPR absorption properties. This property enables AuNPs to produce strong SPR effects under light with a specific wavelength. As creatinine is added to the aqueous solution of AuNPs, a new absorption band is observed at 660 nm. This suggests that the addition of creatinine changes the optical properties of AuNPs, corresponding to the coupling between AuNPs, which causes the SPR absorption band to shift in the direction of longer wavelengths. In SERS experiments, this SPR effect is crucial for enhancing Raman signals. Therefore, when a laser at 633 nm wavelength is used to irradiate AuNPs, a strong SPR effect can be excited. This effect can significantly enhance the Raman scattering signal, thus improving the sensitivity and accuracy of detection, which is consistent with the results of previous studies [27]. This can be confirmed by SERS intensities using excitation lasers with different wavelengths, as shown in Figure S6b.

The SERS performance of the RAuNPs/MXene substrate is evaluated using the R6G molecule with a 633 nm laser, with comparison to that of AuNPs/MXene substrate.

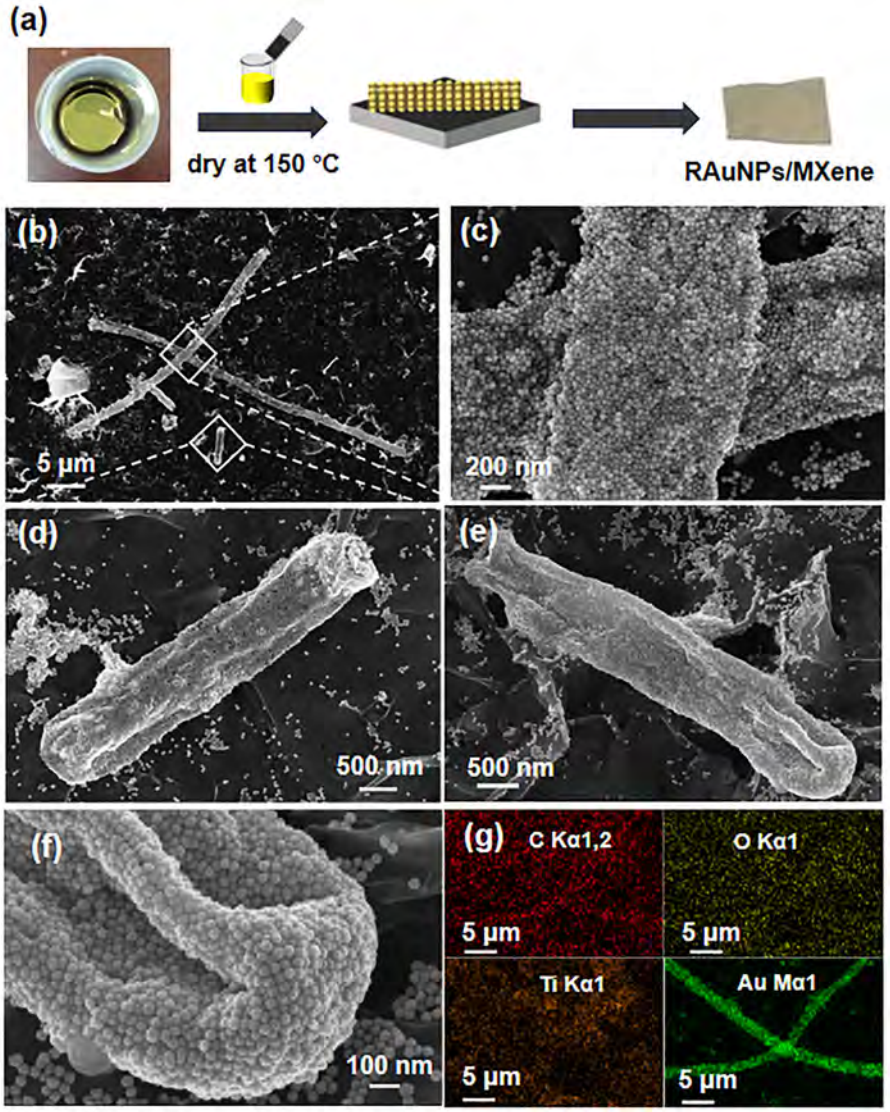

FIGURE 3 | (a) Flow chart showing the preparation process of RAuNPs/MXene; (b–f) scanning electron microscopy (SEM) images of RAuNPs/MXene; and (g) energy-dispersive x-ray spectroscopy (EDS) elemental maps of RAuNPs/MXene. RAuNPs, ribbon-like gold nanoparticle assemblies.

Figure 4a,c shows the Raman spectra collected from the R6G solutions with different concentrations on the AuNPs/MXene and RAuNPs/MXene substrates. The intensity of the typical Raman peaks of R6G at 612 and 774 cm^{-1} decreases with decreasing R6G concentration, and no peak is detected on AuNPs/MXene substrate when the concentration of R6G is 1×10^{-9} M, whereas the lowest detectable concentration is 1×10^{-11} M on RAuNPs/MXene substrate. The corresponding linear relationships between the logarithm of concentration and Raman intensity with the intensity at 774 cm^{-1} as calibration are demonstrated in Figure 4b,d and the error bar representing the standard deviation of three measurements. The empirical equation is $y = 11075 + 1370x$ with R^2 of 0.984 for AuNPs/MXene substrate, and that of RAuNPs/MXene substrate is $y = 36625 + 3401x$ with R^2 of 0.994. The uniformity in detection is also investigated, and the Raman spectra of R6G (1×10^{-6} M) acquired from 10 random regions from the two substrates are illustrated in Figure S7a,b. No significant difference is observed from the peak of 774 cm^{-1} corresponding to a relative standard deviation (RSD) of 7.5% for AuNPs/MXene substrate (Figure 4e) and 6.4% for RAuNPs/MXene substrate (Figure 4f). These results elaborate the excellent SERS performance with better sensitivity and reproducibility of RAuNPs/MXene substrate compared to AuNPs/MXene substrate.

Typically, the 2D MXene is highly electrically conductive, and the abundant CM active sites give it a good metal affinity. The EM field enhancement is most effectively accomplished through a fractal distribution of particles [64]. The densely packed arrangement facilitates intense dipole interactions among the aggregated particles, ultimately leading to prominent SERS signals within the hot spot areas [65]. The functional groups with abundant CM active sites on MXene surface can efficiently interact with AuNPs, leading to the formation of a potent EM field enhancement zone [30]. The banding structures of RAuNPs on MXene surface can cause close contact between MXene layer and AuNPs, leading to the increased number of hot spots in the localized ribbon-like areas [66, 67]. The distinctive RAuNPs can easily and effectively facilitate near-field coupling. In addition, the distinctive ribbon-

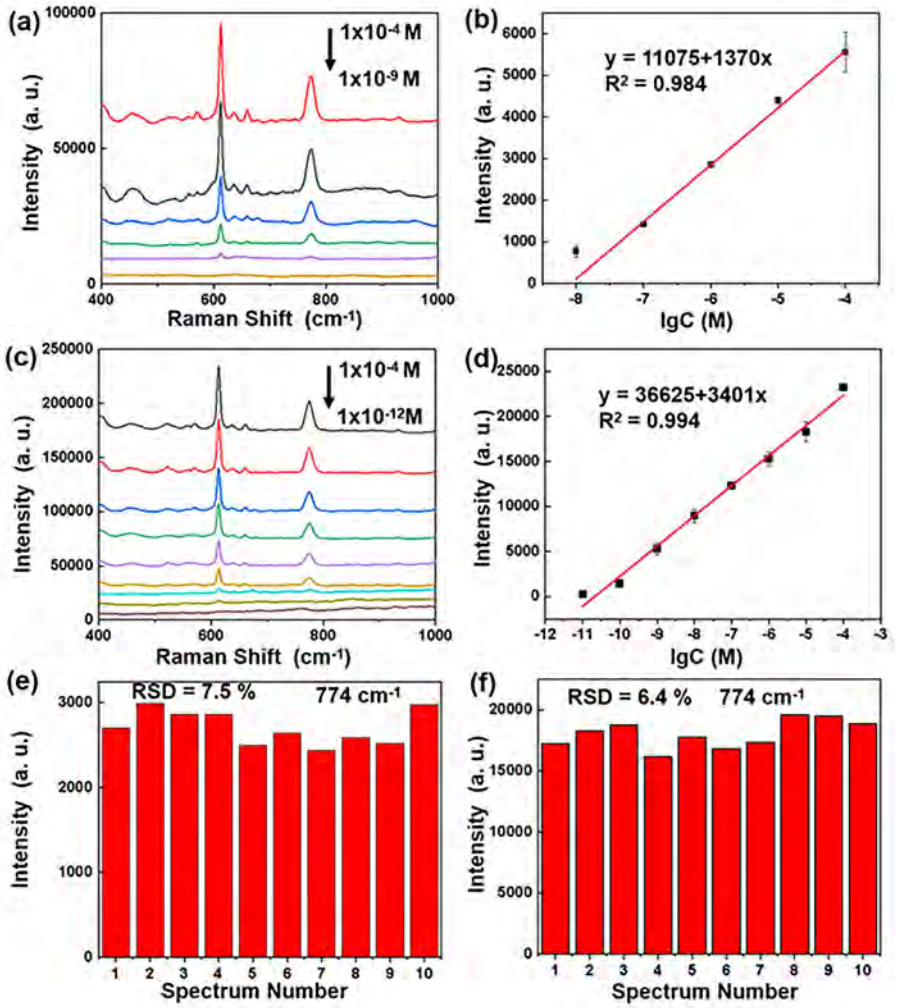

FIGURE 4 | (a) Raman spectra of R6G solutions with different concentrations (1×10^{-4} to 1×10^{-9} M) on AuNPs/MXene substrate, and (b) the corresponding logarithm of concentration versus Raman intensity. (c) Raman spectra of R6G solutions with different concentrations (1×10^{-4} to 1×10^{-12} M) on RAuNPs/MXene substrate, and (d) the corresponding logarithm of concentration versus Raman intensity. Raman intensities at 774 cm^{-1} with the calculated relative standard deviation (RSD) from 10 spectra acquired from the (e) AuNPs/MXene and (f) RAuNPs/MXene substrates, respectively.

like structure is readily observable under an optical microscope, facilitating the target identification. Therefore, RAuNPs/MXene exhibits higher sensitivity than AuNPs/MXene during SERS detection of R6G, and RAuNPs/MXene can be considered an ideal candidate for the construction of high active SERS substrate [68].

To further explore the enhancement effect and mechanism, three different SERS substrates are compared, including AuNPs/Si, AuNPs/MXene, and RAuNPs/MXene, against creatinine molecule. Figure 5a,b shows the Raman spectra of creatinine obtained from AuNPs/MXene and RAuNPs/MXene, respectively, with comparison to those from AuNPs/Si, bare Si substrates, and the creatinine powder as well. The Raman peaks about the vibration information of creatinine powder are usually located at 688, 940, 1428, and 1761 cm^{-1}, respectively [26, 69]. The peak at 688 cm^{-1} is attributed to the inner vibration of the lactam ring of creatinine [70], which is the typical Raman peak used for creatinine detection. The aqueous creatinine solution with a concentration of 1×10^{-2} M is used for the Si substrate, but the Raman signal is very weak. However, the Raman intensity at 688 cm^{-1} is very significant when 1×10^{-6} M is loaded on the three SERS substrates, with the RAuNPs/MXene substrate exhibiting the best signal enhancement effect for creatinine detection. To evaluate the enhancement effect of the three SERS substrates, the analytical enhancement factor (AEF) is calculated by the relationship of $I_{SERS} \times C_{RS}/I_{RS} \times C_{SERS}$ [71], in which I_{SERS} is the Raman peak–peak intensity of creatinine loaded on the SERS substrate, C_{SERS} is the concentration of creatinine (1×10^{-6} M) with the SERS substrate, I_{RS} is the peak–peak intensity of creatinine without the SERS substrate, and C_{RS} is the concentration of creatinine (1×10^{-2} M) without the SERS substrate. By analyzing the Raman peak intensity at 688 cm^{-1} in Figure 5a,b, the AEF values of AuNPs/Si, AuNPs/MXene, and RAuNPs/MXene are determined to be 9.92×10^4, 1.82×10^5, and 5.50×10^5, respectively. Notably, the RAuNPs/MXene substrate exhibits remarkable SERS enhancement, featuring 5.5-fold and 3-fold improvements in AEF compared to AuNPs/Si and AuNPs/MXene substrates, respectively. This substantial improvement is primarily attributed to the plasmonic coupling effect between the MXene and RAuNPs [72]. In addition, MXene

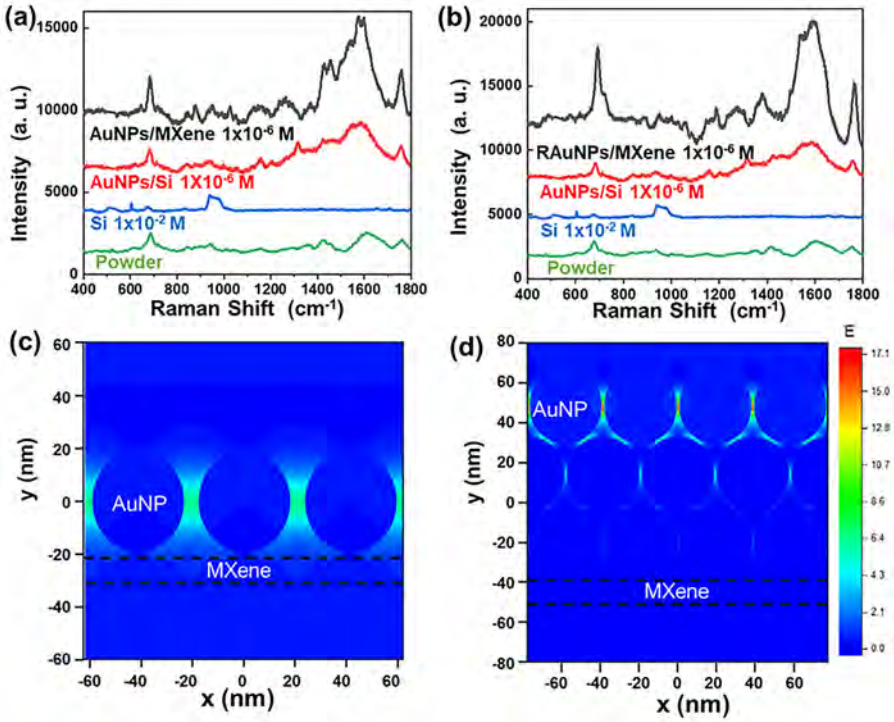

FIGURE 5 | Raman spectra of creatinine (1×10^{-6} M) obtained from the (a) AuNPs/MXene and (b) RAuNPs/MXene substrates, with comparison to those from the AuNPs/Si substrate and bare Si substrate, and numerical simulation of the electromagnetic field enhancement distribution of (c) AuNPs/MXene, and (d) RAuNPs/MXene. RAuNPs, ribbon-like gold nanoparticle assemblies.

also plays a crucial role in the detection process. Its surface is rich in electrons and exhibits excellent electrical conductivity, enabling efficient charge transfer with the molecules adsorbed on it [28, 73]. This efficient charge transfer not only enhances the polarizability of the adsorbed molecules but also increases their Raman scattering cross section, thereby further amplifying the SERS signal [74].

To further investigate the enhancement mechanism associated with EM field distribution, numerical simulation with COMSOL is conducted at a wavelength of 633 nm. As shown in Figure 5c, the EM hotspots in AuNPs/MXene substrate are primarily localized at the nanoscale interstitial gaps between adjacent AuNPs. In contrast, the RAuNPs/MXene substrate with 3D structure and nearer nanoparticle arrangement exhibits EM hotspots concentrated within both the interparticle gaps and interlayer region, where the EM field intensity is markedly enhanced due to plasmonic coupling between adjacent AuNPs layers (Figure 5d). Quantitative comparison of the simulation results demonstrates that the EM field enhancement factor of RAuNPs/MXene is 2.2-fold higher than that of AuNPs/MXene. The numerical simulation further confirms the enhanced EM mechanism, and the better enhancement is consistent with experiment results, underscoring its superior potential for SERS signal amplification.

The excellent SERS performance and enhancement mechanism investigation encourage the SERS detection of creatinine, which is important for the early diagnosis of kidney disease. Both AuNPs/MXene and RAuNPs/MXene can be served as SERS substrates, and a series of creatinine solutions with different concentrations are prepared. Figure 6a shows the Raman spectra of the AuNPs/MXene substrate for different concentrations of creatinine (1×10^{-4} to 1×10^{-8} M). The peak of creatinine at 688 cm^{-1} diminishes gradually with decreasing creatinine concentration. Figure 6b shows the linear relationship between the logarithm of the creatinine concentration and Raman intensity at 688 cm^{-1}. The corresponding empirical fit is $y = 3571 + 553x$ with R^2 of 0.867. Figure 6c shows the Raman spectra of creatinine (1×10^{-6} M) measured from 10 randomly selected spots, revealing an RSD of 22.5%, as shown in Figure 6d. Figure 7a shows the Raman spectra for different creatinine concentrations (1×10^{-3} to 1×10^{-10} M) measured from RAuNPs/MXene substrate. The intensity of the peak at 688 cm^{-1} decreases gradually with decreasing creatinine concentration, and Figure 7b shows the linear relationship between the logarithm of the creatinine concentration and Raman intensity at 688 and 944 cm^{-1}, with the equation of $y = 5287 + 423x$ ($R^2 = 0.991$) and $y = 1619 + 176x$ ($R^2 = 0.762$), respectively. The linear relationship observed between Raman intensity and concentration at 688 cm^{-1} is superior to that at the peak value of 944 cm^{-1}. Consequently, the SERS intensity measured at 688 cm^{-1} was selected for quantitative determination. Figure 7c shows the Raman spectra of creatinine (1×10^{-6} M) measured from 20 randomly selected areas of MXene/RAuNPs. Figure 7d shows an RSD of 5.1%, indicating good consistency and reliability. For the same creatinine concentration, the RSD of RAuNPs/MXene (5.1%) is smaller than that of AuNPs/MXene (22.5%). As shown in Figures S8a and 8b, with the storage time of 1 day, 15 days, and 47 days, the signal intensity acquired from the RAuNPs/MXene substrate demonstrates only slight change. After 47 days, the peak intensity reduces only by 14.6%, and the intensity from different batches varied slightly, with the reproducibility of 6.58% (Figure S8c). The results demonstrate good stability

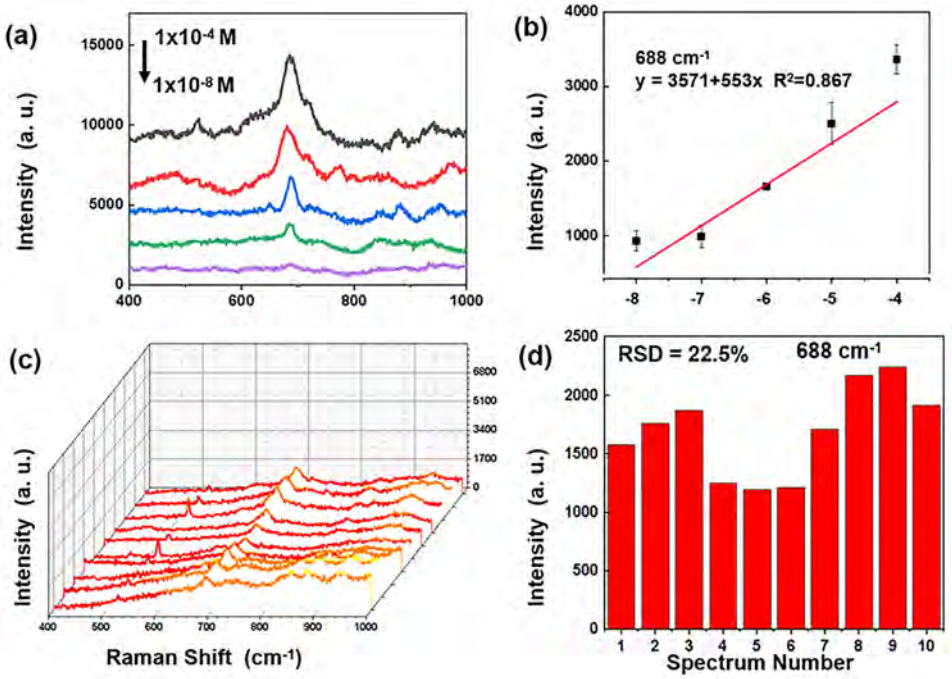

FIGURE 6 | (a) Raman spectra of different concentrations of creatinine (1×10^{-4} to 1×10^{-8} M) acquired from the AuNPs/MXene substrate; (b) logarithm of creatinine concentration versus the Raman intensity at 688 cm^{-1} (error bar representing the standard deviation of three measurements); (c) Raman spectra of creatinine (1×10^{-6} M) measured at 10 random points on the AuNPs/MXene substrate; and (d) relative standard deviation (RSD) of 22.5% calculated from the 10 Raman spectra at 688 cm^{-1}.

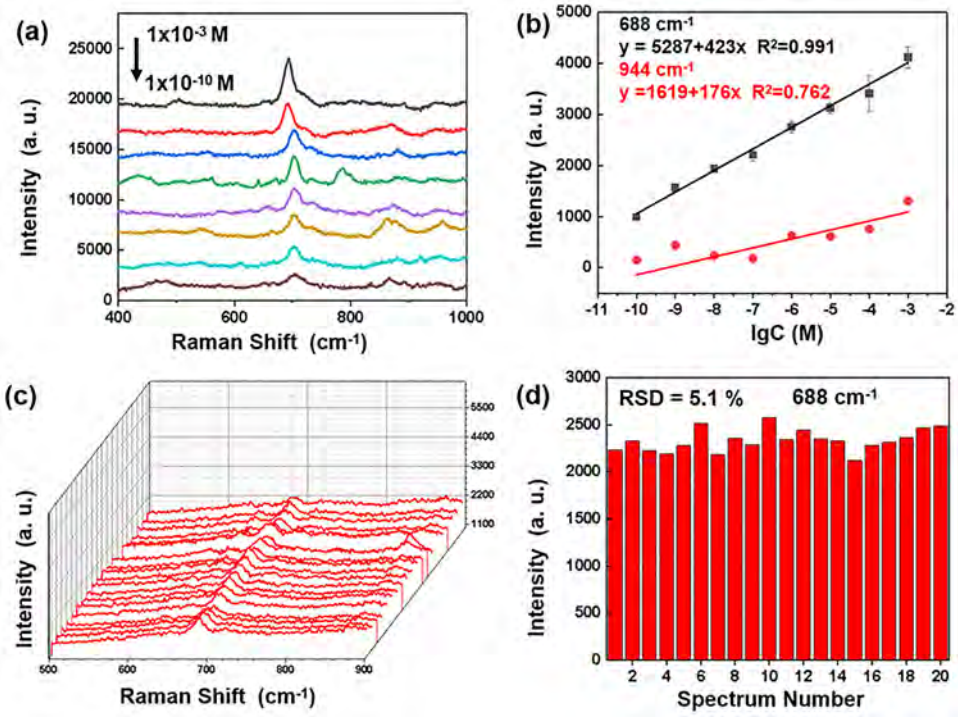

FIGURE 7 | (a) Raman spectra of regions with different creatinine concentrations (1×10^{-3} to 1×10^{-10} M) acquired from the RAuNPs/MXene substrate; (b) logarithm of creatinine concentration versus Raman intensity at 688 and 944 cm^{-1} (error bar representing the standard deviation of three measurements); (c) Raman spectra of creatinine (1×10^{-6} M) acquired from 20 random points on RAuNPs/MXene; and (d) relative standard deviation (RSD) of 5.1% calculated from 20 Raman spectra at 688 cm^{-1}.

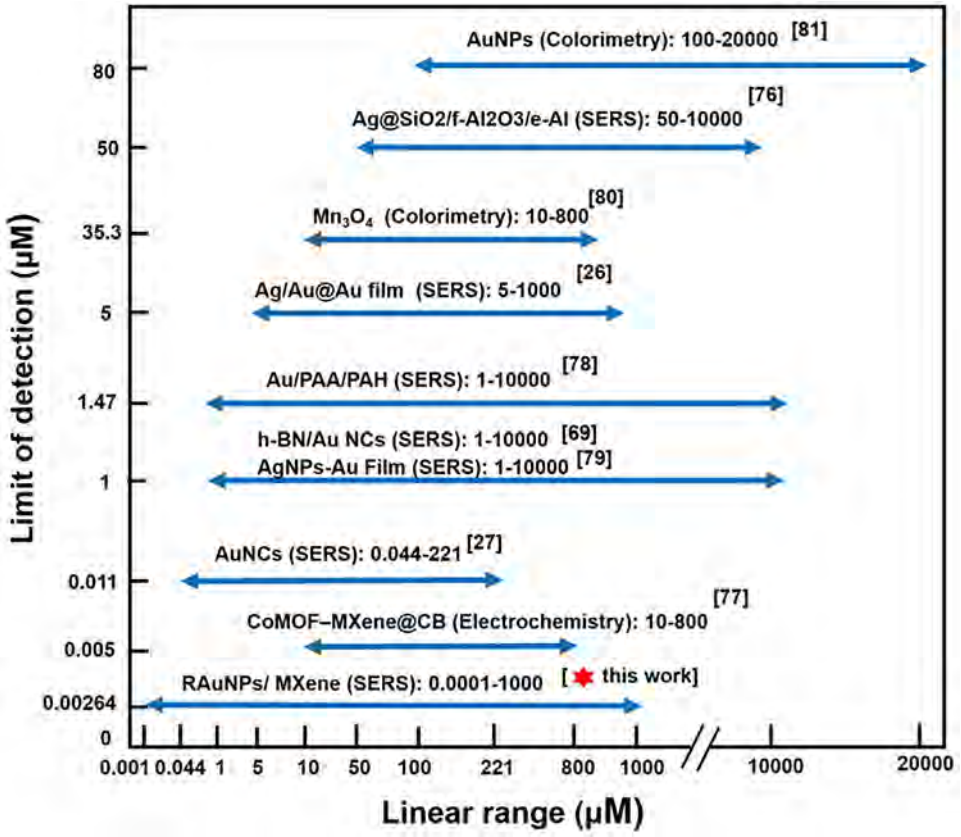

FIGURE 8 | Comparison of creatinine detection performance of RAuNPs/MXene with other surface-enhanced Raman scattering (SERS) substrates and detection techniques. RAuNPs, ribbon-like gold nanoparticle assemblies.

and reproducibility, providing strong support for its reliability in practical applications.

Both the SERS substrates exhibit high degree of correlation across the different ranges of creatinine concentration, demonstrating the good SERS activity. Specifically, the detection limit of creatinine by AuNPs/MXene is 1×10^{-8} M with R^2 of 0.867, whereas the RAuNPs/MXene substrate shows a detection limit of 1×10^{-10} M with R^2 of 0.991. The LOD is calculated using the formula LOD = 3Sd/k [75]. In this equation, Sd represents the standard deviation of Raman signal intensities obtained from 10 replicate measurements of the blank RAuNPs/MXene composite substrate, and k is the slope of the linear calibration curve at 688 cm^{-1} shown in Figure 7b. This method statistically defines the minimum reliably detectable concentration at a signal-to-noise ratio (SNR) of approximately 3. As a result, the LOD of the two SERS substrates are calculated to be 287 and 2.64 nM, respectively. These LOD values confirm the superior sensitivity of the RAuNPs/MXene substrate.

As shown in Figure 8, which compares the detection sensitivity of creatinine using various techniques, including SERS [26], [27, 69, 76–81], the RAuNPs/MXene 3D SERS substrate developed in this study exhibits the lowest LOD of 2.64 nM, with a linear detection range spanning from 10^{-3} to 10^{-10} M. Compared to other reported SERS substrates, this substrate demonstrates higher sensitivity within its linear range. Furthermore, coupled with optical microscopy for rapid localization of target detection areas, it significantly enhances detection efficiency. These results indicate that the RAuNPs/MXene 3D SERS substrate holds considerable promise for trace substance detection.

In order to demonstrate the specificity of the RAuNPs/MXene SERS substrate for creatinine detection, three typical molecules in serum, including ascorbic acid, uric acid, and glucose, are selected as the interferences. Creatinine and the three interferences can be detected at a low concentration of 1×10^{-6} M. As shown in Figure 9a, only the creatinine molecule displays a significant signal enhancement, whereas the other three interferences show no detectable signal. That is, the three interference molecules do not interfere with the creatinine signal during SERS measurement. It is confirmed that the RAuNPs/MXene SERS substrate has a certain degree of selectivity for creatinine. Figure 9b displays the SERS spectra of three serum samples detected on RAuNPs/MXene. In advance, the creatinine concentrations of the three serum samples have been measured by clinical enzymatic method, of which the tested values are 133, 52, and 49 μM, respectively. Subsequently, the RAuNPs/MXene substrate is performed for the SERS measurement to the same serum samples. According to the linear equation of 688 cm^{-1} peak value as shown in Figure 7b, the creatinine concentrations of the three serum samples are measured and calculated as 115, 45, and 40 μM, respectively. Figure 9c displays the detection results by two different methods, and the relative error of SERS measurement compared to the enzymatic method is also calculated. Finally, the mean relative error is calculated as 11.6%. It is indicated that the creatinine detection by RAuNPs/MXene SERS substrate exhibits good specificity and high accuracy.

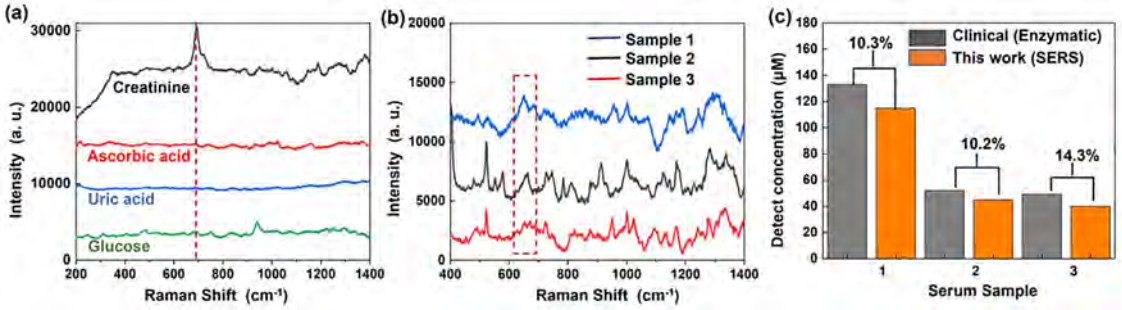

FIGURE 9 | (a) Comparison of surface-enhanced Raman scattering (SERS) spectra between creatinine and the other three interferences (ascorbic acid, uric acid, and glucose); (b) SERS spectra of the three serum samples detected on RAuNPs/MXene substrate; and (c) the detection results compared between the clinical method and this work.

4 | Conclusion

Homogeneous ultrathin Ti_3C_2-MXene films are fabricated on a large scale by the interfacial self-assembly method. By simply regulating the assembly condition, the uniformly distributed AuNPs and 3D ribbon-like assemblies are separately assembled on the MXene surface. The combined structure of MXene layers and AuNPs provides many active sites and hot spots to facilitate SERS detection. The two SERS substrates of AuNPs/MXene and RAuNPs/MXene are compared regarding the detection of creatinine in aqueous solutions without labels, and the SERS activity is verified by the Raman probe molecule of R6G. In the SERS detection of creatinine, the AuNPs/MXene substrate exhibits a linear range from 10^{-4} to 10^{-8} M with a LOD of 287 nM, whereas the RAuNPs/MXene shows a linear relationship from 10^{-3} to 10^{-10} M with a LOD of 2.64 nM. The detection LOD creatinine by RAuNPs/MXene is better than that by AuNPs/MXene, furnishing evidence that the combined substrate delivers better SERS performance and suggesting promising potential in the rapid and sensitive detection of creatinine.

Author Contributions

Lin Chen: conceptualization, data curation, formal analysis, methodology, writing – original draft. **Dong Yang**: formal analysis, software, writing – review and editing. **Wanlin Wang**: supervision, software. **Hongyun Xing**: supervision, software. **Xianglong Bian**: methodology. **Hua Pei**: methodology, resources, validation. **Qianfeng Xia**: supervision. **Penghui Li**: formal analysis, writing – review, editing. **Paul K. Chu**: formal analysis, writing – review and editing, funding acquisition. **Tingwei Hu**: conceptualization, data curation, formal analysis, funding acquisition, project administration, supervision, writing – review and editing.

Acknowledgments

This work was jointly supported by the National Natural Science Foundation of China (No. 82472150), the Hainan Provincial Natural Science Foundation of China (No. 521RC555), Talent Researching Funds (XRC200016, RC2400001279), City University of Hong Kong Donation Research Grants (DON-RMG 9229021 and 9220061), and Hainan Medical University Research Foundation (XSTS2025033).

Conflicts of Interest

The authors declare no conflicts of interest.

Data Availability Statement

The data that support the findings of this study are available on request from the corresponding author. The data are not publicly available due to privacy or ethical restrictions.

Peer Review

The peer review history for this article is available at: https://publons.com/publon/10.1111/nyas.70097.

References

1. T. Liyanage, T. Ninomiya, V. Jha, et al., "Worldwide Access to Treatment for End-Stage Kidney Disease: A Systematic Review," *Lancet* 385, no. 9981 (2015): 1975–1982.

2. N. Greenberg, W. L. Roberts, L. M. Bachmann, et al., "Specificity Characteristics of 7 Commercial Creatinine Measurement Procedures by Enzymatic and Jaffe Method Principles," *Clinical Chemistry* 58, no. 2 (2012): 391–401.

3. X. Guo, L. Hou, X. Cheng, et al., "Strong Negative Interference by Calcium Dobesilate in Sarcosine Oxidase Assays for Serum Creatinine Involving the Trinder Reaction," *Medicine* 94, no. 23 (2015): e905.

4. T. Zhang, X. Guo, L. Hou, et al., "Effects of Calcium Dobesilate (CaD) Interference on Serum Creatinine Measurements: A National External Quality Assessment (EQA)-Based Educational Survey of Drug-Laboratory Test Interactions," *Clinical Chemistry and Laboratory Medicine* 59, no. 1 (2021): 139–145.

5. J. C. Thakur and D. Hazarika, "Clinical Analysis and Detection of Creatinine by Conventional Methods and Electrochemical Biosensors: A Review," *IEEE Sensors Journal* 24, no. 1 (2024): 16–27.

6. W. Lee, B. H. Kang, H. Yang, et al., "Spread Spectrum SERS Allows Label-Free Detection of Attomolar Neurotransmitters," *Nature Communications* 12, no. 1 (2021): 159.

7. J. Li, Y. Feng, L. Liang, et al., "Flexible Multicavity SERS Substrate Based on Ag Nanoparticle-Decorated Aluminum Hydrous Oxide Nanoflake Array for Highly Sensitive In Situ Detection," *ACS Applied Materials & Interfaces* 16, no. 27 (2024): 35771–35780.

8. B. Q. Du, J. B. Tan, C. Ji, et al., "Thermoelectric Field-Assisted Raman Scattering and Photocatalysis With GaN-Plasmonic Metal Composites," *ACS Photonics* 10, no. 7 (2022): 2216–2225.

9. P. Mao, C. Liu, G. Favraud, et al., "Broadband Single Molecule SERS Detection Designed by Warped Optical Spaces," *Nature Communications* 9, no. 1 (2018): 5428.

10. P. Liu, X. Y. Zhu, T. Xue, et al., "A Novel Graphene-Like Titanium Carbide MXene/Au–Ag Nanoshuttles Bifunctional Nanosensor for Electrochemical and SERS Intelligent Analysis of Ultra-Trace Carbendazim Coupled With Machine Learning," *Ceramics International* 47, no. 1 (2021): 173–184.

11. X. Chen, M. Lin, L. Sun, et al., "Detection and Quantification of Carbendazim in Oolong Tea by Surface-Enhanced Raman Spectroscopy and Gold Nanoparticle Substrates," *Food Chemistry* 293 (2019): 271–277.

12. T. Bai, A. Otitoju, T. Sun, et al., "Highly Sensitive In Situ SERS Monitoring of Fenton-Like Reaction by a PDDA-MXene@AuNP Composite," *New Journal of Chemistry* 47, no. 11 (2023): 5174–5178.

13. K. Wang and J. Li, "Reliable SERS Detection of Pesticides With a Large-Scale Self-Assembled Au@4-MBA@Ag Nanoparticle Array," *Spectrochimica Acta Part A* 263 (2021): 120218–120218.

14. X. Cui, J. Li, Y. Li, et al., "Detection of Glucose in Diabetic Tears by Using Gold Nanoparticles and MXene Composite Surface-Enhanced Raman Scattering Substrates," *Spectrochimica Acta Part A* 266, no. 0 (2022): 120432.

15. Y. Peng, C. Lin, L. Long, et al., "Charge-Transfer Resonance and Electromagnetic Enhancement Synergistically Enabling MXenes With Excellent SERS Sensitivity for SARS-CoV-2 S Protein Detection," *Nano-Micro Letters* 13, no. 3 (2021): 1–17.

16. L. Liu, C. Shangguan, J. Guo, et al., "Ultrasensitive SERS Detection of Cancer-Related miRNA-182 by MXene/MoS_2@AuNPs With Controllable Morphology and Optimized Self-Internal Standards," *Advanced Optical Materials* 8, no. 23 (2020): 2001214.

17. X. Guo, Y. Li, B. Ye, et al., "Rapid Label-Free SERS Detection of Foodborne Pathogenic Bacteria Based on Hafnium Ditelluride-Au Nanocomposites," *Journal of Innovative Optical Health Sciences* 13, no. 5 (2020): 2041004.

18. Y. T. Yeh, K. Gulino, Y. Zhang, et al., "A Rapid and Label-Free Platform for Virus Capture and Identification From Clinical Samples," *Proceedings of the National Academy of Sciences* 117, no. 2 (2019): 895–901.

19. D. Cialla-May, A. Bonifacio, T. Bocklitz, et al., "Biomedical SERS: The Current State and Future Trends," *Chemical Society Reviews* 53 (2024): 8957–8979.

20. S. Y. Ding, E. M. You, Z. Q. Tian, et al., "Electromagnetic Theories of Surface-Enhanced Raman Spectroscopy," *Chemical Society Reviews* 46, no. 13 (2017): 4042–4076.

21. L. R. Madison, C. M. Aikens, G. C. Schatz, et al., "The Effect of Field Gradient on SERS," *Nature Photonics* 7, no. 7 (2013): 508–510.

22. S. D. Qiao, Y. H. Liu, C. Fang, et al., "A Highly Sensitive LITES Sensor Based on a Multi-Pass Cell With Dense Spot Pattern and A Novel Quartz Tuning Fork With Low Frequency," *Opto-Electronic Advances* 7, no. 3 (2024): 230230–230230.

23. Y. J. Jang, J. Kim, N. J. Kim, et al., "Study of Chemical Enhancement Mechanism in Non-Plasmonic Surface- Enhanced Raman Spectroscopy (SERS)," *Frontiers in Chemistry* 7 (2019): 582.

24. C. Ji, M. R. Shao, J. B. Tan, et al., "Ferroelectrically Modulate the Fermi Level of Graphene Oxide to Enhance SERS Response," *Opto-Electronic Advances* 6, no. 11 (2023): 230094–230094.

25. M. Magdy, "A Conceptual Overview of Surface-Enhanced Raman Scattering (SERS)," *Plasmonics* 18, no. 2 (2023): 803–809.

26. P. Wen, F. Yang, C. Ge, et al., "Self-Assembled Nano-Ag/Au@Au Film Composite SERS Substrates Show High Uniformity and High Enhancement Factor for Creatinine Detection," *Nanotechnology* 32, no. 39 (2021): 395502.

27. L. Z. Su, L. Zhang, Y. Zhou, et al., "Quantitative Detection of Creatinine in Human Serum by SERS With Evaporation-Induced Optimal Hotspots on Au Nanocubes," *ACS Applied Nano Materials* 5, no. 4 (2022): 4841–4847.

28. S. Z. Qu, Y. X. Zhao, H. S. Kang, et al., "Plasmon Coupling and Efficient Charge Transfer in Rough-Surfaced Au Nanotriangles/MXene Hybrids as an Ultrasensitive Surface-Enhanced Raman Scattering Platform," *ACS Omega* 7, no. 51 (2022): 48438–48446.

29. Y. H. Kuo, Y. L. Miao, S. F. Zong, et al., "Au/Ag Bimetallic Nanocuboid Superlattices Coated With Ti_3C_2 Nanosheets for Surface-Enhanced Raman Spectroscopy Detection of Fish Drug Residues in Pond Water," *ACS Applied Nano Materials* 4, no. 7 (2021): 6844–6851.

30. T. Maleski, M. Sarycheva, K. Satheeshkumar, and E. Melikyan, "Two-Dimensional Titanium Carbide (MXene) as Surface-Enhanced Raman Scattering Substrate," *Journal of Physical Chemistry C* 121, no. 36 (2017): 19983–19988.

31. M. B. Bhavya, A. Patra, G. Manasa, et al., "2D MXenes as a Promising Candidate for Surface-Enhanced Raman Spectroscopy: State of the Art, Recent Trends, and Future Prospects," *Advanced Functional Materials* 33, no. 42 (2023): 2306680.

32. A. VahidMohammadi, J. Rosen, and Y. Gogotsi, "The World of Two-Dimensional Carbides and Nitrides (MXenes)," *Science* 372, no. 6547 (2021): eabf1581.

33. Y. L. Deng, J. Y. Zhang, L. F. Chen, et al., "A Novel Electrochemiluminescence Aptasensor Using Ti_3C_2@AuNRs-Ru for Ultra-Sensitive Detection of T-2 Toxin," *Electrochimica Acta* 475 (2024): 143688.

34. Y. Shao, W. Deng, Y. Niu, et al., "Synergistic Enhancement of the Ag/ZIF-67 Cage@MXene 3D Heterogeneous Structure for Ultrahigh SERS Sensitivity and Stability," *Analyst* 150, no. 6 (2025): 1131–1139.

35. H. H. Xie, P. H. Li, J. D. Shao, et al., "Electrostatic Self-Assembly of $Ti_3C_2T_x$ MXene and Gold Nanorods as an Efficient Surface-Enhanced Raman Scattering Platform for Reliable and High-Sensitivity Determination of Organic Pollutants," *ACS Sensors* 4, no. 9 (2019): 2303–2310.

36. Z. Yang, L. Yang, Y. Liu, et al., "Photocatalytic Deposition of Au Nanoparticles on $Ti_3C_2T_x$ MXene Substrates for Surface-Enhanced Raman Scattering," *Molecules (Basel, Switzerland)* 29, no. 10 (2024): 2383.

37. M. J. Kim, R. Manikandan, H. G. Jang, et al., "Fabrication of Bio-Mimic Nanozyme Based on Mxene@AuNPs and Molecular Imprinted Poly(thionine) Films for Creatinine Detection," *Biosensors & Bioelectronics* 271 (2025): 1–7.

38. Y. Li, Y. Hang, R. Gopali, et al., "Point-of-Care Testing Device Platform for the Determination of Creatinine on an Enzyme@CS/PB/MXene@AuNP-Based Screen-Printed Carbon Electrode," *Microchimica Acta* 191, no. 9 (2024): 1–13.

39. L. Ma, K. Zhou, X. Wang, et al., "Recent Progress in the Synthesis of 3D Complex Plasmonic Intragap Nanostructures and Their Applications in Surface-Enhanced Raman Scattering," *Biosensors* 14, no. 9 (2024): 433.

40. M. K. Hossain, Q. A. Drmosh, and A. K. Mohamedkhair, "Plasmonic Pollen Grain Nanostructures: A Three-Dimensional Surface-Enhanced Raman Scattering (SERS)-Active Substrate," *Chemistry—An Asian Journal* 16, no. 13 (2021): 1807–1819.

41. N. Zhao, H. Li, Y. Xie, et al., "3D Aluminum/Silver Hierarchical Nanostructure With Large Areas of Dense Hot Spots for Surface-Enhanced Raman Scattering," *Electrophoresis* 40, no. 23–24 (2019): 3123–3131.

42. Y. Zhang, H. Wang, C. Ni, et al., "Three-Dimensional Nanoporous Gold/Gold Nanoparticles Substrate for Surface-Enhanced Raman Scattering Detection of Illegal Additives in Food," *Spectrochimica Acta Part A* 323 (2024): 124879.

43. D. Qu, Y. Jian, L. Guo, et al., "An Organic Solvent-Assisted Intercalation and Collection (OAIC) for $Ti_3C_2T_x$ MXene With Controllable Sizes and Improved Yield," *Nano-Micro Letters* 13, no. 1 (2021): 1–13.

44. S. J. Kim, J. Choi, K. Maleski, et al., "Interfacial Assembly of Ultrathin, Functional MXene Films," *ACS Applied Materials & Interfaces* 11, no. 35 (2019): 32320–32327.

45. D. Tu, A. Holderby, and G. L. Coté, "Aptamer-Based Surface-Enhanced Resonance Raman Scattering Assay on a Paper Fluidic Platform for Detection of Cardiac Troponin," *Journal of Biomedical Optics* 25, no. 9 (2020): 097001–097001.

46. R. Sanim, "Size and Concentration Analysis of Gold Nanoparticles With Ultraviolet-Visible Spectroscopy," *Undergraduate Journal of Mathematical Modeling: One + Two* 7, no. 1 (2016): 1–15.

47. X. Wang, S. G. Park, J. Ko, et al., "Sensitive and Reproducible Immunoassay of Multiple Mycotoxins Using Surface-Enhanced Raman Scattering Mapping on 3D Plasmonic Nanopillar Arrays," *Small* 14, no. 39 (2018): e1801623.

48. S. L. Murray, S. Serajian, and S. I. Gnani Peer Mohamed, "Ultrabroadband Optical Properties of 2D Titanium Carbide MXene," *ACS Applied Materials & Interfaces* 16, no. 51 (2024): 70763–70773.

49. S. Agarwal, R. Kumar, S. Pal, et al., "Refractive Index Sensing Using MXene Mediated Surface Plasmon Resonance Sensor in Visible to Near Infrared Regime," *Measurement* 224 (2024): 113682.

50. J. Shim, J. M. Yun, T. Yun, et al., "Two-Minute Assembly of Pristine Large-Area Graphene Based Films," *Nano Letters* 14, no. 3 (2014): 1388–1393.

51. F. Wu, P. Hu, F. Hu, et al., "Multifunctional MXene/C Aerogels for Enhanced Microwave Absorption and Thermal Insulation," *Nano-Micro Letters* 15, no. 1 (2023): 194.

52. T. Hu, J. Wang, H. Zhang, et al., "Vibrational Properties of Ti_3C_2 and $Ti_3C_2T_2$(T = O, F, OH) Monosheets by First-Principles Calculations: A Comparative Study," *Physical Chemistry Chemical Physics* 17, no. 15 (2015): 9997–10003.

53. M. Chaput, N. Presser, L. Togi, et al., "Erratum: First-Order Raman Scattering of the MAX Phases: Ti_2AlN, $Ti_2AlC_{0.5}N_{0.5}$, Ti_2AlC, $(Ti_{0.5}V_{0.5})_2AlC$, V_2AlC, Ti_3AlC_2, and Ti_3GeC_2," *Journal of Raman Specroscopy* 44, no. 7 (2013): 1060–1060.

54. X. Liu, A. Dang, T. Li, et al., "Triple-Enhanced Raman Scattering Sensors From Flexible MXene/Au Nanocubes Platform via Attenuating the Coffee Ring Effect," *Biosensors and Bioelectronics* 237 (2023): 115531–115531.

55. T. Wei, L. C. Liu, X. Guan, et al., "Size and Morphology Adjustment of PVP-Stabilized Silver and Gold Nanocrystals Synthesized by Hydrodynamic Assisted Self-Assembly," *Journal of Physical Chemistry C* 113, no. 20 (2009): 8595–8600.

56. O. Mashtalir, M. Naguib, V. N. Mochalin, et al., "Intercalation and Delamination of Layered Carbides and Carbonitrides," *Nature Communications* 4 (2013): 1716.

57. W. Wu, Z. X. Zheng, T. Yang, et al., "In Situ Reduced MXene/AuNPs Composite Toward Enhanced Charging/Discharging and Specific Capacitance," *Journal of Advanced Ceramics* 10, no. 5 (2021): 1061–1071.

58. M. Naguib, V. N. Mochalin, M. W. Barsoum, et al., "25th Anniversary Article: MXenes: A New Family of Two-Dimensional Materials," *Advanced Materials* 26, no. 7 (2013): 992–1005.

59. W. H. Ni, N. Pazos-Pérez, A. Schweikart, et al., "Highly Uniform SERS Substrates Formed by Wrinkle-Confined Drying of Gold Colloids," *Chemical Science* 1, no. 2 (2010): 174–178.

60. Z. Y. Kuai, W. Peng, P. Jin, et al., "MXene-Based Gold Nanoparticle Catalyst With High Activity and Stability for 4-Nitrophenol Reduction," *Journal of Solid State Chemistry* 325 (2023): 124166.

61. H. Pan, S. Low, N. Weerasuriya, et al., "Morphological Transformation of Gold Nanoparticles on Graphene Oxide: Effects of Capping Ligands and Surface Interactions," *Nano Convergence* 6, no. 1 (2019): 2.

62. E. Baños-López, Y. M. Hernández-Rodríguez, P. Damián-Matsumura, et al., "The Influence of Temperature on the Spatial Distribution of AuNPs on a Ceramic Substrate for Biosensing Applications," *Chemosensors* 12, no. 10 (2024): 212.

63. A. Glamazda, E. Usenko, A. Svidzerskal, et al., "DNA-TiO_2 Nanoparticle Nanoassembies: Effect of Temperature and Nanoparticles Concentration on Aggregation," *Journal of Nanoparticle Research* 25, no. 6 (2023): 1–14.

64. Z. Wang, S. Pan, T. D. Krauss, et al., "The Structural Basis for Giant Enhancement Enabling Single-Molecule Raman Scattering," *Proceedings National Academy of Science USA* 100, no. 15 (2003): 8638–8643.

65. A. Damin, A. P. Budnyk, G. Agostini, et al., "Gold Nanoparticle Aggregates Immobilized on High Surface Area Silica Substrate for Efficient and Clean SERS Applications," *Journal of Physical Chemistry C* 114, no. 9 (2010): 3857–3862.

66. J. Ho, S. S. Yoo, D. I. Shin, et al., "Simultaneously Intensified Plasmonic and Charge Transfer Effects in Surface-Enhanced Raman Scattering Sensors Using an MXene-Blanketed Au Nanoparticle Assembly," *Journal of Materials Chemistry A* 10, no. 6 (2022): 2945–2956.

67. B. Fazio, C. D'Andrea, A. Foti, et al., "SERS Detection of Biomolecules at Physiological PH via Aggregation of Gold Nanorods Mediated by Optical Forces and Plasmonic Heating," *Scientific Reports* 6, no. 1 (2016): 26952.

68. Z. W. Liu, G. Wang, Y. F. Li, et al., "Substrate Types and Applications of MXene for Surface-Enhanced Raman Spectroscopy," *Frontiers in Chemistry* 12 (2024): 1378985.

69. G. H. Li, H. Zhang, S. Li, et al., "Boron Nitride/Gold Nanocomposites for Crystal Violet and Creatinine Detection by Surface-Enhanced Raman Spectroscopy," *Applied Surface Science* 457 (2018): 684–694.

70. S. Mishra, K. Vikram, S. K. Srivastava, et al., "Low Temperature Raman and DFT Study of Creatinine," *Journal of Molecular Structure* 1012 (2012): 141–150.

71. B. K. Sahu, M. K. Francis, P. B. Bhargav, et al., "Ag Nanowires Based SERS Substrates With Very High Enhancement Factor," *Physica E* 137 (2022): 115080.

72. X. Liu, A. Dang, T. Li, et al., "Plasmonic Coupling of Au Nanoclusters on a Flexible MXene/Graphene Oxide Fiber for Ultrasensitive SERS Sensing," *ACS Sensors* 8, no. 3 (2023): 1287–1298.

73. M. B. Chitara, T. B. Limbu, Y. G. Cervantes, et al., "Unravelling the Thickness Dependence and Mechanism of Surface-Enhanced Raman Scattering on $Ti_3C_2T_x$ MXene Nanosheets," *Journal of Physical Chemistry C* 124, no. 32 (2020): 17772–17782.

74. A. L. Dang, Y. H. Liu, X. Liu, et al., "Recyclable MXene Film as SERS Sensor With High Sensitivity and Flexibility Adjusted With ZnO Quantum Dots," *Sensors and Actuators B: Chemical* 422 (2025): 136685.

75. I. B. Ansah, S. H. Lee, C. Mun, et al., "Galvanic Engineering of Interior Hotspots in 3D Au/Ag Bimetallic SERS Nanocavities for Ultrasensitive and Rapid Recognition of Phthalate Esters," *Chemical Engineering Journal* 470 (2023): 144161.

76. M. K. Nguye, W. N. Su, and B. J. Hwang, "A Plasmonic Coupling Substrate Based on Sandwich Structure of Ultrathin Silica-Coated Silver Nanocubes and Flower-Like Alumina-Coated Etched Aluminum for Sensitive Detection of Biomarkers in Urine," *Advanced Healthcare Materials* 6, no. 10 (2017): 1601290.

77. D. Roy, R. Singh, S. Mandal, et al., "An MXene-Supported Cobalt-MOF Nanocomposite-Printed Electrochemical Sensor With High Sensitivity for Blood Creatinine Detection in Point-of-Care Settings," *Analytical Methods* 16, no. 36 (2024): 6183–6192.

78. A. Ngamaroonchote and K. Karn-orachai, "Role of Polyelectrolyte Multilayers Over Gold Film for Selective Creatinine Detection Using Raman Spectroscopy," *Applied Surface Science* 546 (2021): 149092.

79. F. Yang, P. Wen, G. Li, et al., "High-Performance Surface-Enhanced Raman Spectroscopy Chip Integrated With a Micro-Optical System for the Rapid Detection of Creatinine in Serum," *Biomedical Optics Express* 12, no. 8 (2021): 4795–4806.

80. Y. Lu, N. Shen, Y. Xi, et al., "Bioenzyme-Free Colorimetric Assay for Creatinine Determination Based on Mn_3O_4 Nanoparticles Catalyzed Oxidation of 3,3′,5,5′-Tetramethylbenzidine," *Microchimica Acta* 191, no. 1 (2023): 44.

81. X. H. Zhang, Y. He, and H. L. Yu, "Gold Nanoparticles-Based Colorimetric and Visual Creatinine Assay," *Microchimica Acta* 182, no. 11–12 (2015): 2037–2043.

Supporting Information

Additional supporting information can be found online in the Supporting Information section.

Supplementary Figures: nyas70097-sup-0001-FigureS1–S8.doc

Supporting Information

Three-dimensional Ribbon-like Gold Nanoparticles Assemblies on MXene for Detection of Creatinine by Surface-Enhanced Raman Scattering

Lin Chen[1,#], Dong Yang[2,#], Wanlin Wang[3], Hongyun Xing[3], Xianglong Bian[1], Hua Pei[1], Qianfeng Xia[1], Penghui Li[4,*], Paul K. Chu[5,*], Tingwei Hu[1,*]

[1] *NHC Key Laboratory of Tropical Disease Control, School of Tropical Medicine, Hainan Medical University, Haikou 571199, Hainan, China*

[2] *School of Biomedical Information and Engineering, Hainan Medical University, Haikou 571199, Hainan, China*

[3] *School of Physical Sciences, Great Bay University, Dongguan 523000, China*

[4] *Institute of Biomedicine and Biotechnology, Shenzhen Institutes of Advanced Technology, Chinese Academy of Sciences, Shenzhen 518055, China*

[5] *Department of Physics, Department of Materials Science and Engineering, and Department of Biomedical Engineering, City University of Hong Kong, Tat Chee Avenue, Kowloon, Hong Kong, China*

# Lin Chen and Dong Yang contributed equally to this work and should be considered as co-first authors.

* Address correspondence to: htingwei1236@mail.xjtu.edu.cn (Tingwei Hu) ph.li@siat.ac.cn (Penghui Li) and paul.chu@cityu.edu.hk (Paul K. Chu)

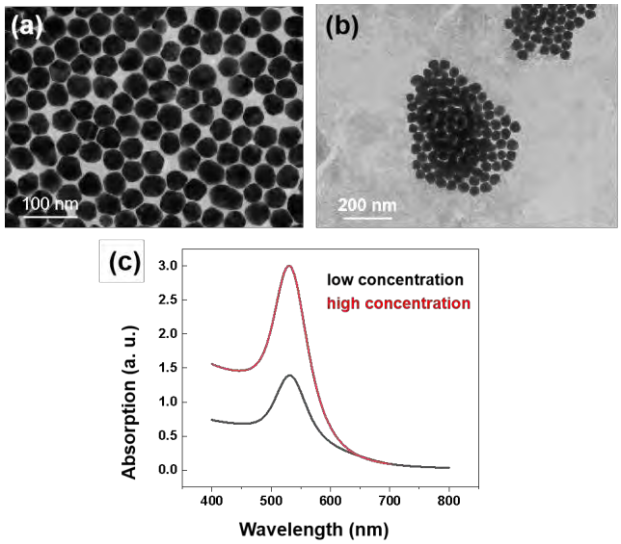

Figure S1. (a, b) TEM images of AuNPs in different aggregate states; (c) Typical UV-visible absorption spectrum of low and high concentration AuNPs solution.

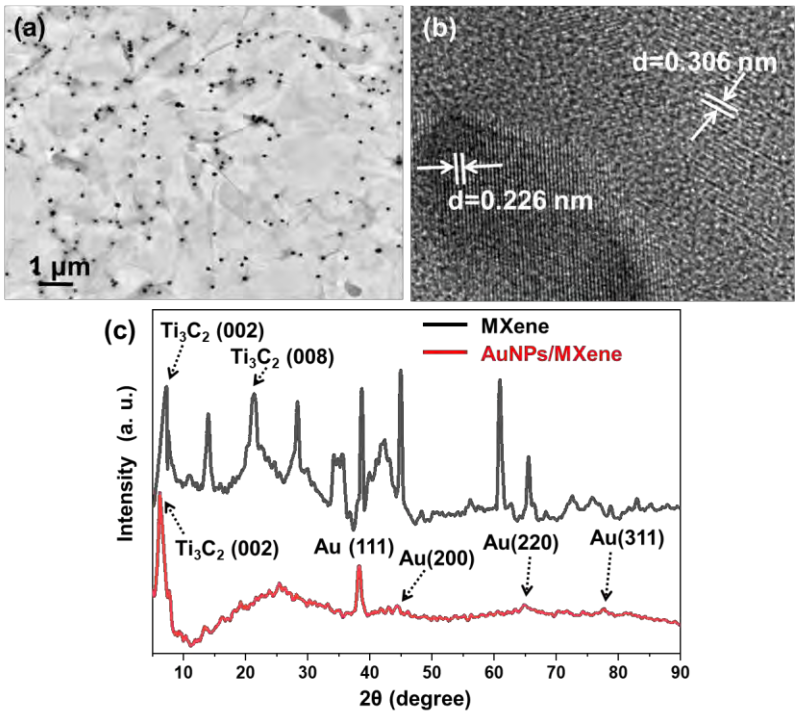

Figure S2. (a, b) TEM and HR-TEM images of AuNPs/MXene; (c) XRD spectra of MXene films (black) and AuNPs/MXene (red).

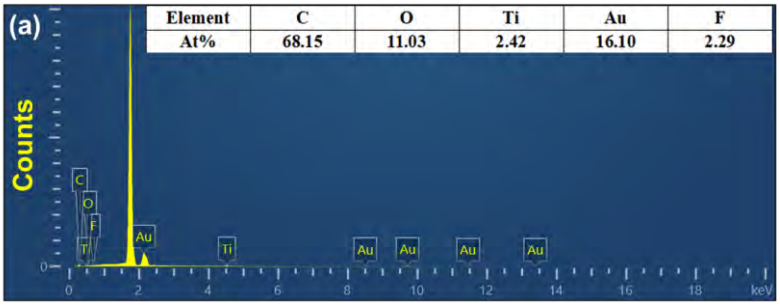

Figure S3. EDS elemental spectrum with elemental contents of AuNPs/MXene.

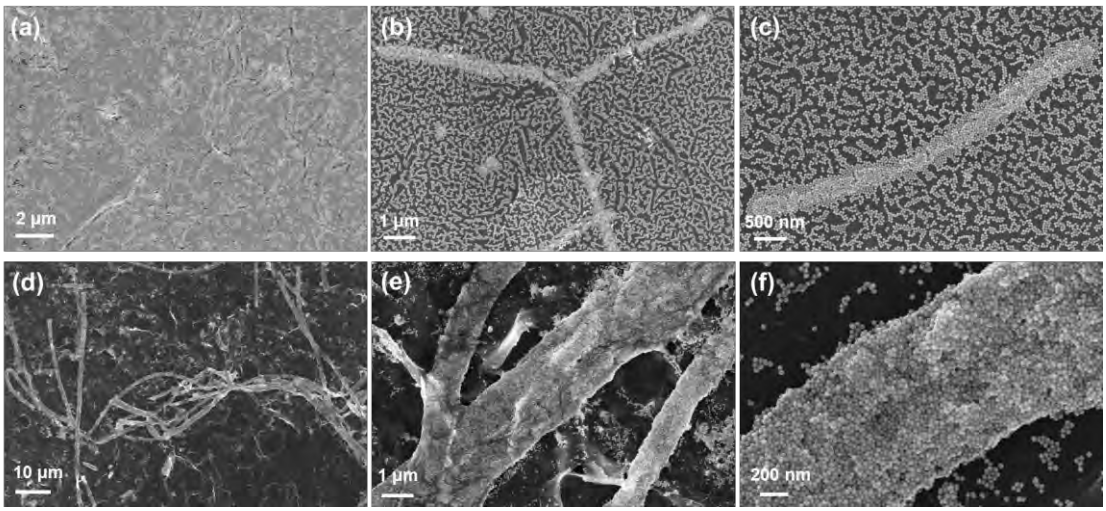

Figure S4. (a-c) SEM images of dispersed RAuNPs/MXene obtained from low concentration AuNPs solution; (d-f) SEM images of densely packed RAuNPs/MXene obtained from high concentration AuNPs solution.

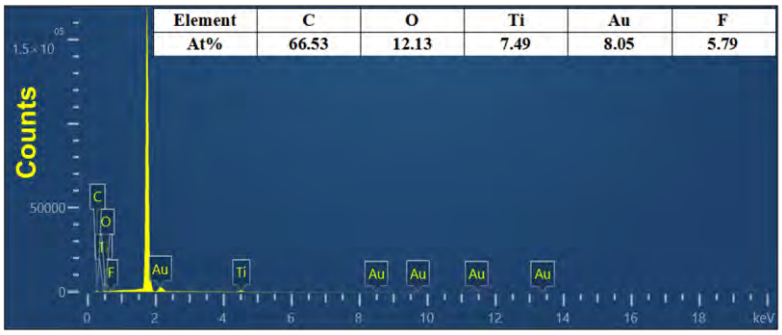

Figure S5. EDS elemental spectrum with elemental contents of RAuNPs/MXene.

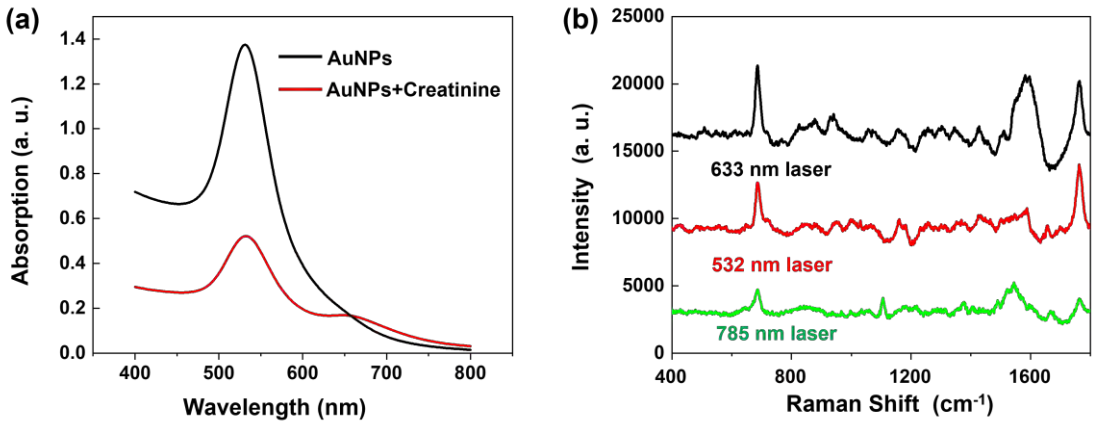

Figure S6. (a) UV-visible absorption spectra of AuNPs and creatinine mixed with AuNPs. (b) SERS spectra of creatinine acquired on RAuNPs/MXene using excitation laser with different wavelengths.

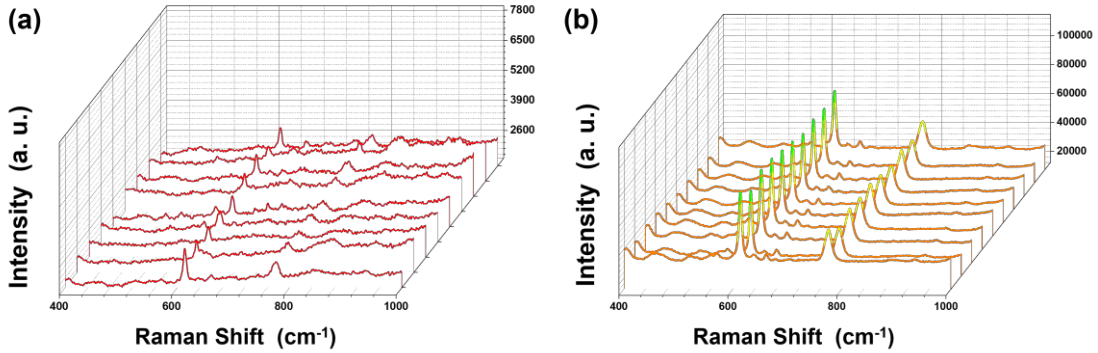

Figure S7. SERS spectra of R6G (1×10^{-6} M) acquired from 10 random points on AuNPs/MXene (a) and RAuNPs/MXene (b).

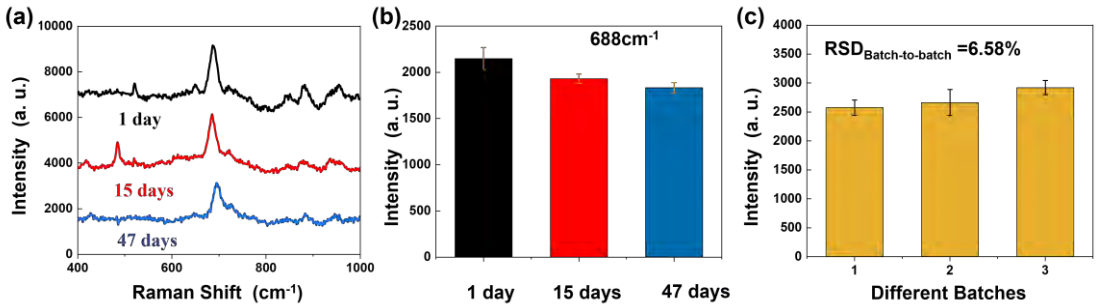

Figure S8. The stability of the RAuNPs/MXene SERS substrates: (a) SERS spectra of creatinine (1×10^{-8} M) acquired from RAuNPs/MXene with different storage times; (b) The Raman peak intensities at 688 cm^{-1} from Fig. S8a (n=3); (c) The Raman peak intensities of creatinine (1×10^{-6} M) at 688 cm^{-1} (n = 3) from substrates prepared in different batches representing the batch-to-batch.